Lab on a Chip

Accepted Manuscript

ROYAL SOCIETY OF CHEMISTRY

www.rsc.org/loc

Journal Name

ARTICLE TYPE

Cite this: DOI: 10.1039/xxxxxxxxxx

Microfluidics Droplet Trapping, Splitting and Merging with Feedback Controls and State Space Modelling†

David Wong and Carolyn L. Ren[a]

Received Date
Accepted Date

DOI: 10.1039/xxxxxxxxxx

www.rsc.org/journalname

We combine image processing and feedback controls to regulate droplets movements. A general modelling approach is provided to describe droplets motion in a pressure-driven microfluidic channel network. A state space model is derived from electric circuit analogy, and validated with experimental data. We then design simple decentralized controllers to stabilize droplets movement. The controllers can trap droplets at requested locations by fine tuning inlet pressures constantly. Finally, we demonstrate the ability to split and merge the same droplet repeatedly in a simple T-junction. No embedded electrodes are required, and this technique can be implemented solely with a camera, a personal computer, and commercially available E/P transducers.

1 Introduction

Recently, droplet microfluidics have found applications in biochemical research such as DNA amplification[1], cell cultivation and RNA transcription[2], and have demonstrated advantages acting as reactors for nano-particles[3] and hydrogel[4] synthesis.

Among these applications, the ability to split and merge droplets is critical for triggering chemical reactions and making concentration adjustment. In addition, droplet trapping is essential for incubation, detection, and making observations.

Existing methods for droplet manipulation such as Electro-Wetting-On-Dielectric[5] often complicates chip fabrication by introducing electrodes, or requires external acoustic or optical equipment[6] that would potentially interfere with biochemical processes. While passive splitting and merging[7] has been proven possible, they only work within a narrow range of operating conditions[8], and is susceptible to downstream disturbance and fabrication defects.

Piotr Garstecki, leading researcher in droplet microfluidics, has demonstrated the potential of automated droplet-based system, and applied the technology in screening biochemical reactions[9,10] and creating vast libraries of distinct chemical environments[11]. Garstecki's group has developed automated droplet-on-demand platforms[12] that are capable of generating, spiting, merging, and circulating droplets. By manually regulating inlet pressures, and using information from image processing to trigger valve opening sequences, their system can achieve complicated procedures required in maintaining chemostats, where individual droplets has to be repeatedly screened, split to dispose of waste volume, and merged with replenishment nutrients. They have also studied the droplet splitting accuracy, and applied the system to study growth dynamics of *E coli* under different medium.

In this study, we provide a general state space model that describes droplets movement in a pressure-driven microfluidics channel network. Through image processing feedback and pressure actuation, the user is given freedom to move droplets independent of each other, and to place them at arbitrary locations. In addition, upstream or downstream disturbance, as well as effects due to fabrication defects are compensated by the closed-loop system.

Controls theory has been applied to microfluidics before. Miller[13] and Zeng[14] used feedback control to regulate droplet sizes, but have no ability to adjust size independent of spacing, nor the ability to control individual droplets. Kuczenski[15] and Kim[16] applied feedback controls on a syringe pump and a peristaltic device, in order to regulate concentration in a two phase flow. Their focus was on manipulating the laminar interface, rather than controlling droplet motion. Using embedded electrodes, Niu[17] was able to sense droplet presence and perform open-loop sorting. Movements of suspended particles in single phase flow has also been studied. Armani[18] demonstrated the ability to steer particles using multiple electrodes, while Shenoy[19] utilized model predictive control and pressure actuation to manipulate particle movements.

The modelling and controls techniques used in this study are well established, and widely documented in text books such as Woods[20] and Franklin[21].

[a] *Mechanical and Mechatronics Engineering, University of Waterloo 200, University Avenue West, Waterloo, Canada. Tel: +1 519 888 4567; E-mail: c3ren@uwaterloo.ca*

† Electronic Supplementary Information (ESI) available: [details of any supplementary information available should be included here]. See DOI: 10.1039/b000000x/

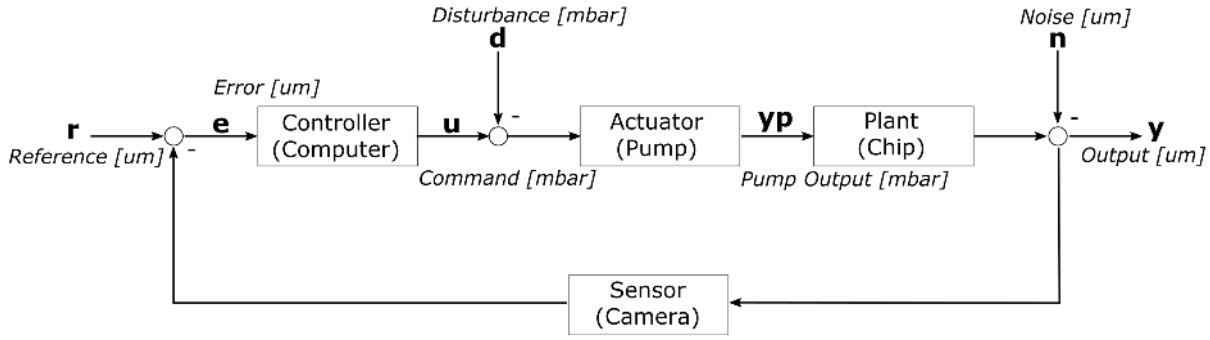

Fig. 1 A typical SISO feed-back topology.

Table 1 List of Variables

Variables	Unit	Description
r	μm	Controller Reference
e	μm	Controller Error
u	$mbar$	Controller Command
d	$mbar$	Disturbance
y	μm	Output
y_p	μm	Pump Model Output
n	μm	Noise
s		Laplace Transform Parameter
z		Z Transform Parameter
P_*, C_*		Plant, Controller Transfer Function
R	$mbar \cdot s/\mu m$	Resistance
L	$mbar \cdot s^2/\mu m$	Inductance
C	$\mu m/mbar$	Capacitance
$\triangle P$	$mbar$	Pressure Difference
v	$\mu m/s$	Flow Velocity
x	μm	Flow Displacement
ρ	kg/m^3	Density
μ	$kg/m*s$	Dynamic Viscosity
κ	N/m	Material Stiffness
β	Pa	Adiabatic Bulk Modulus
V	m^3	Channel Volume
A	m^2	Cross-section Area
l	m	Channel Length
d_h	m	Hydraulic Diameter

2 Methdology

A typical closed-loop Single-Input-Single-Output (SISO) system is shown in figure 1. The actuator block contains pump dynamics, attained from system identification. The plant block represents droplet dynamics in a microfluidics channel network. At any point in time, reference r represents the user requested droplet position, while output y represents the actual droplet position, captured by camera and measured through image processing. The goal of this system is to match output y to reference r, and this is achieved by designing a controller. When given an error $e = r - y$, the controller provides an appropriate command u, which actuates the pump to deliver pressure y_p, and results in the desirable droplet movements.

Furthermore, a good controller can minimize the influence of disturbance d, which comes from un-modelled dynamics; and reject noise n caused by external stimulus. For illustration convenience, the SISO topology shown in figure 1 is a simplification of the topic at hand, hiding the fact that droplet dynamics is a Multi-Input-Multi-Output (MIMO) system, where changing one inlet pressure will affect flow in multiple channels. A more realistic topology would involve multiple figure 1 stacking on top of each other with interconnected signals, and r, e, u, d, y, etc. were all vectors of different lengths.

2.1 Pressure Pump

For this study, a Fluigent MFCS-EZ pressure pump is used. The pressure pump has four electro-pneumatic transducers with proprietary pressure regulation technology. As shown in figure 2B, when given a step input command u, pressure output y_p takes time to response, then overshoot before settling to the requested value.

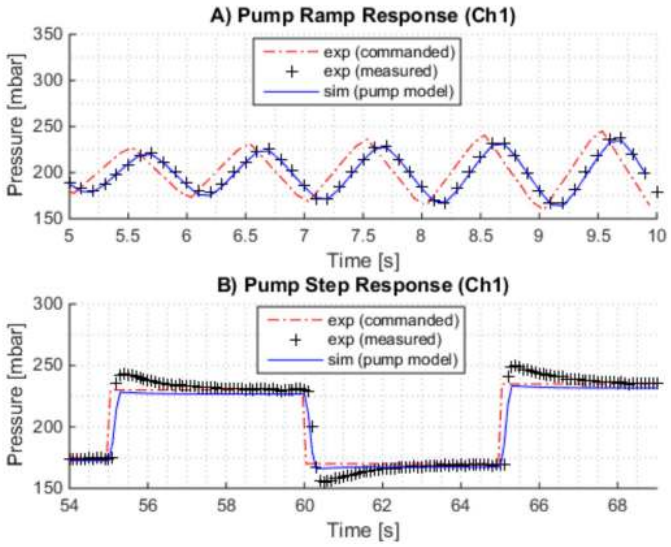

Fig. 2 System identification of pressure pump

Without knowledge of the transducers' proprietary technology, modelling of the pump behaviour would be difficult. Instead, system identification techniques are used to approximate pump behaviour.

$$\overbrace{\begin{bmatrix} y_p(0) \\ y_p(-T) \\ y_p(-2T) \\ \dots \end{bmatrix}}^{Y} = \overbrace{\begin{bmatrix} y_p(-T) & \dots & y_p(-3T) & u(0) & ,,, & u(-3T) \\ y_p(-2T) & \dots & y_p(-4T) & u(-T) & ,,, & u(-4T) \\ y_p(-3T) & \dots & y_p(-5T) & u(-2T) & ,,, & u(-5T) \\ \dots & \dots & \dots & \dots & \dots & \dots \end{bmatrix}}^{\Psi} \overbrace{\begin{bmatrix} \alpha_1 \\ \alpha_2 \\ \alpha_3 \\ \beta_0 \\ \beta_1 \\ \beta_2 \\ \beta_3 \end{bmatrix}}^{\Theta} + \overbrace{\begin{bmatrix} e(0) \\ e(-T) \\ e(-2T) \\ \dots \end{bmatrix}}^{E} \quad (1)$$

$$\Theta = (\Psi^T \Psi)^{-1} \Psi^T Y \quad (2)$$

$$P_{pump} = \frac{y_p(z)}{u(z)} = \frac{\beta_0 + \beta_1 z^{-1} + \beta_2 z^{-2} + \beta_3 z^{-3}}{1 - \alpha_1 z^{-1} + \alpha_2 z^{-2} + \alpha_3 z^{-3}} \quad (3)$$

First, pressure pump was connected to reservoir that is half-full and sealed to simulate normal operating conditions. Ramp, step, or sinusoidal signal of increasing amplitude and frequency was commanded as shown in figure 2A. Command and measurement was assigned as $u(t)$ and $y_p(t)$ into equation 1, where T is sampling period, Y is a vector of measurement over time, Ψ is the regression matrix composed of previous data, Θ contains model variables of interest, and E represents fitting error. Provided that $\Psi^T\Psi$ is invertible, model variables Θ can be found by minimizing E using least square regression (equation 2). The resulting pump model P_{pump} is listed in equation 3, where z is the Z transform parameter.

It was found that model variables obtained from ramp data do not provide good prediction of step response (figure 2B) nor frequency response . This suggests that pump dynamics is nonlinear. A compromise was made and equation 4 is used in the rest of this study. More sophisticated system identification technique would be needed to improve pump model later.

$$P_{pump} = \frac{0.132z^{-1} + 0.3441z^{-2}}{1 - 0.5847z^{-1} + 0.06081z^{-2}}$$
$$SamplePeriod = 0.1 \quad (4)$$

The pump is controlled by computer through USB with a proprietary communication protocol. The protocol limits communication to $10Hz$ (for each channel), forcing the controllers and the rest of the closed-loop system to operate at a sampling period of no less than $0.1s$.

2.2 Camera and Image Processing

The Andor Zyla 5.5 scientific camera is capable of streaming 5.5 mega-pixel images at $40Hz$. In the experiment, however, image resolution is reduced to 0.26 mega-pixel (512×512) in order to reduce computation work load from image processing. While the controllers and pump operate at $10Hz$, camera is set up to stream at $40Hz$ in order to reduce acquisition delay. Comparison between image time-stamp and computer clock suggested that acquisition delay averages at $50ms$, which can be fully absorbed into the $0.1s$ sampling period.

Image processing was performed in MATLAB; standard edge detection methods were used; image erosion and dilation were used to eliminate pixel noise. Figure 4 shows droplet boundary and water-oil interface being detected and highlighted, while droplet centroid are plotted on top of the raw image.

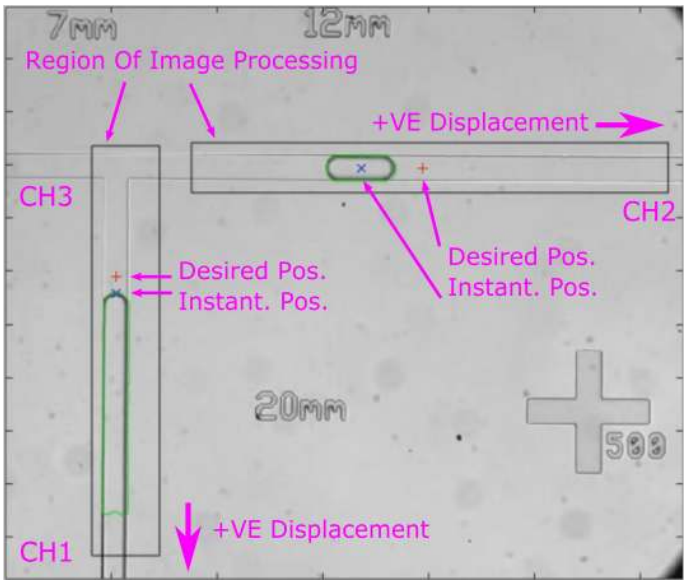

Fig. 3 Black boxes enclose regions where image processing takes place, edges of droplets are detected in real time and plotted as green, fluid interface and droplet centroid is marked blue, while controller reference r (user demand) is marked red. For illustration purpose, chip with channel width of $100\mu m$ is shown. Please note that data presented in this paper are obtained from chips with channel width of $50\mu m$. see table 2 for details.

2.3 Microfluidic Chip

The microfluidic chips were made of PDMS, and fabricated using standard soft-lithography techniques[22]. Table 2 lists channel dimensions and material properties that are used throughout this study. Water and $50cSt$ oil are used as the dispersed and continuous phase, no surfactant are used.

Referring to figure 4. Channel 1 supplies the dispersed phase, while the continuous phase flows from channel 2 to channel 3 or from channel 3 to channel 2, depending applied pressures. In addition to the T-junction, a $500\mu m$ cross-hair is fabricated along for image-processing calibration.

3 Modelling

Transient fluid motion in a control volume (CV) is governed by conservation of momentum and mass, while steady state flow is described by the Hagen-Poiseuille law that governs laminar flow. Reynolds Transport Theorem can relate those CV laws of conservation to system forces, resulting in dynamics similar to mass spring dampers.

By assuming that these inertia, stiffness, and damping effects are linear and unrelated to each other, they can be modelled separately using electric circuit analogy, and later added together using the superposition properties of linear systems. Furthermore, under the assumption that fluid flow inside a channel is uniform and 1-dimensional, and that droplets move at the same speed as the surrounding continuous phase, droplet dynamics can be described with such fluid model. The advantage of electric circuit analogy lies in its ability to scale up and describe vast interconnected networks.

3.1 Electric Circuit Analogy

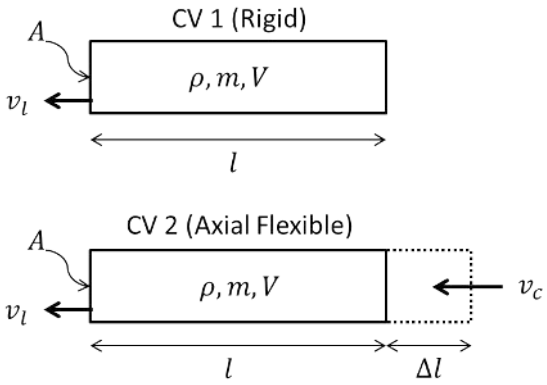

Fig. 4 Control Volumes move and accelerate with fluid

Under the linear system assumption, a fluid element is represented by two separate CVs that moves and accelerate with fluid flow. The first CV is rigid, contains incompressible fluid, and models inertia effects. The second CV is axial flexible and models effects of compliance. Those two effects are combined through superposition of droplet velocity $v = v_l + v_c$.

Applying conservation of momentum with Reynolds transport theorem on the first CV results in equation 5. Since CV1 is rigid and incompressible, the flux term can be eliminated, resulting in equation 6. Substituting $net force$ with pressure difference $\triangle P$ and cross section area A results in equation 7. Making the analogy that voltage and current is pressure difference and velocity, inductance L of the fluid element can be calculated from equation 8

$$\frac{d}{dt}\int \rho \cdot v_l dV = \int \frac{\partial}{\partial t}(\rho \cdot v_l)dV + flux \tag{5}$$

$$net force = \frac{d}{dt}(m \cdot v_l) = m \cdot \dot{v_l} + \dot{m} \cdot v_l \tag{6}$$

$$\triangle P \cdot A = \rho \cdot l \cdot A \cdot \dot{v_l} \tag{7}$$

$$L = \frac{\triangle P}{\dot{v_l}} = \rho \cdot l \tag{8}$$

Applying conservation of mass to CV2 yields equation 9. By neglecting $\frac{\partial \rho}{\partial t}$, and substituting $net flux = \rho \cdot A \cdot v_c$, equation 10 is obtained. Describing change of fluid density with adiabatic bulk modulus β results in equation 11, which is then integrated w.r.t time to get equation 12. Finally, applying Hooke's Law $\triangle l = \frac{\triangle P \cdot A}{\kappa}$ where stiffness κ is derived from young modulus of chip material, equation 13 is obtained. The relationship between droplet displacement and pressure difference can be described as capacitance (equation 14).

$$\frac{d}{dt}\int \rho dV = \int \frac{\partial \rho}{\partial t} dV + flux \tag{9}$$

$$\frac{d}{dt}(\rho \cdot V) = \rho \cdot \dot{V} + \dot{\rho} \cdot V = \rho \cdot A \cdot v_c \tag{10}$$

$$\rho \cdot (A \cdot \dot{l}) + (\frac{\rho}{\beta}\frac{d \triangle P}{dt}) \cdot A \cdot l = \rho \cdot A \cdot v_c \tag{11}$$

$$A \cdot \triangle l + \frac{\triangle P \cdot A \cdot l}{\beta} = A \cdot x_c \tag{12}$$

$$\triangle P(\frac{A}{\kappa} + \frac{l}{\beta}) = x_c \tag{13}$$

$$C = \frac{x_c}{\triangle P} = \frac{A}{\kappa} + \frac{l}{\beta} \tag{14}$$

Finally, the Hagen-Poiseuille law (equation 15)is used to derive resistance, which describes damping effects of the fluid element.

$$R = \frac{\triangle P}{v} = \frac{32 \cdot \mu \cdot l}{d_h^2} \tag{15}$$

Channel and tubing dimensions used in this study, as well as numerical values of resistance, inductance, and capacitance are given in table 2.

Table 2 Model Parameters Value

Parameters	Channel 1	Channel 2	Channel 3
Chip			
Height(μm)	50	50	50
Width (μm)	50	50	50
Length (mm)	20	12	7
R ($mbar \cdot s/\mu m$)	2.56e-3	73.9e-3	43.1e-3
L ($mbar \cdot s^2/\mu m$)	0.200e-6	0.116e-6	0.0674e-6
C ($\mu m/mbar$)	0.934e-3	0.991e-3	0.578e-3
Tubing			
Radius (μm)	127	381	381
Length (mm)	490	490	490
R ($mbar \cdot s/\mu m$)	2.43e-3	13.0e-3	13.0e-3
L ($mbar \cdot s^2/\mu m$)	4.90e-6	4.72e-6	4.72e-6
C ($\mu m/mbar$)	34.7e-3	151e-3	151e-3
Fluid	water	oil (50 cSt)	oil (50 cSt)

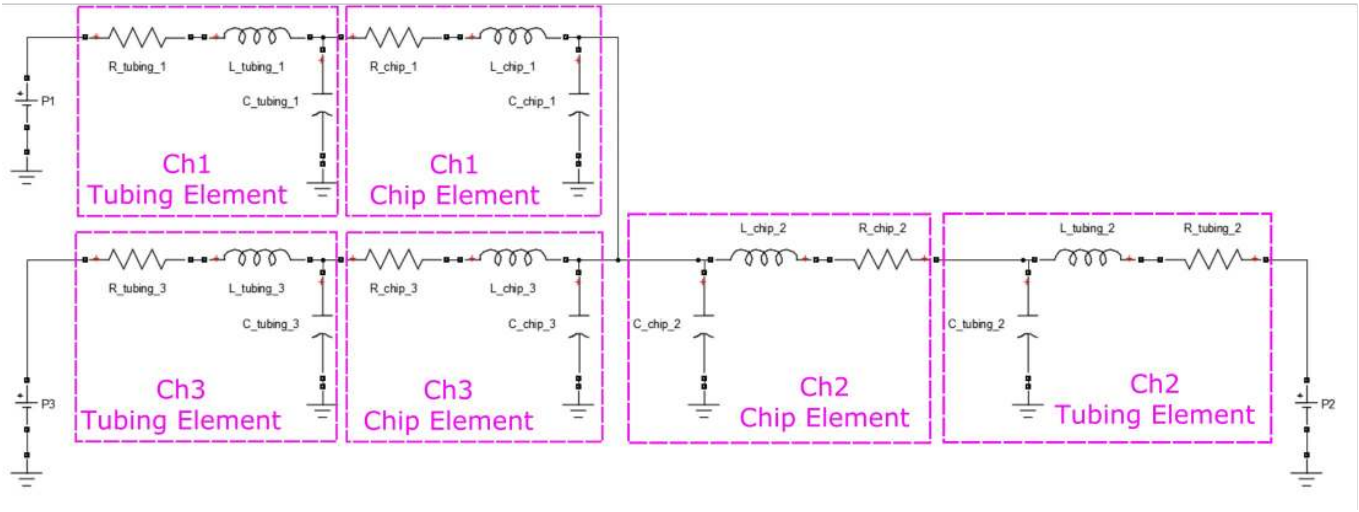

Fig. 5 A circuit representation of the T-junction, including tubings connecting chip to pump reservoirs

3.2 Microfluidic Channel Network

Applying circuit analogy to microfluidics channel network, figure 5 shows a circuit representation of the T-junction used in this study. Each hardware component (connection tubing, microfluidic channel) is represented by one fluid element. Within each element, a resistor and inductor is connected in series, under the reasoning that pressure drop $\triangle P$ is contributed by both laminar flow and fluid inertia. Each fluid element is also connected to ground by a capacitor, where ground represents atmospheric pressure. The Capacitor "charges up" as PDMS expands, and fluid compresses.

The representation shown in Figure 5 is by no means the most accurate. For example, opposite current passing through a fluid element will experience slightly different $\triangle P$ due to the asymmetric placement of the capacitor. This can be solved by using more than one fluid element for each hardware component (finite-element approach), at the expense of model complexity. Furthermore,in the event where significant slippage occur between droplets and continuous phase, or when droplets occupy a major portion of a supposedly continuous-phase-filled channel, the model derived from figure 5 will no longer be valid. In such case, a Linear Time Varying model can be developed, where state space matrices are updated in real-time base on information from additional image processing.

With the circuit representation in place, it remains to extract the chip state space model (A_c, B_c, C_c, D_c) that describes droplet dynamics versus inlet pressures. A differential equation is written for each fluid element, and the system of ODEs is algebraically manipulated into state space form. For example, a hand derived state space model for a simplified T-junction (no tubing, no Capacitors) is shown in equation 16, in which x denote droplet displacement, v denote droplet velocity, P denote inlet pressure, R and L denote resistance and inductance, and subscripts $(1,2,3)$ refer to the channel/element to whom the parameters belong.

$$\overbrace{\begin{bmatrix}\dot{x_3}\\ \dot{x_2}\\ \dot{x_1}\\ \dot{v_2}\\ \dot{v_1}\end{bmatrix}}^{\dot{x_c}} = \overbrace{\begin{bmatrix} 0 & 0 & 0 & -1 & -1 \\ 0 & 0 & 0 & 1 & 0 \\ 0 & 0 & 0 & 0 & 1 \\ 0 & 0 & 0 & \frac{R_1+R_2-R_1L_1/(L_1+L_3)}{L_1+L_2-(L_1^2/(L_1+L_3))} & \frac{R_1-L_1(R_1+R_3)/(L_1+L_3)}{L_1+L_2-(L_1^2/(L_1+L_3))} \\ 0 & 0 & 0 & \frac{R_1-L_1(R_1+R_2)/(L_1+L_2)}{L_1+L_3-L_1^2/(L_1+L_3)} & \frac{R_1+R_3-R_1L_1/(L_1+L_2)}{L_1+L_3-L_1^2/(L_1+L_3)} \end{bmatrix}}^{A_c} \overbrace{\begin{bmatrix}x_3\\ x_2\\ x_1\\ v_2\\ v_1\end{bmatrix}}^{x_c} + \overbrace{\begin{bmatrix} 0 & 0 & 0 \\ 0 & 0 & 0 \\ 0 & 0 & 0 \\ \frac{L_1/(L_1+L_3)-1}{L_1+L_2-(L_1^2/(L_1+L_3))} & \frac{1}{L_1+L_2-(L_1^2/(L_1+L_3))} & \frac{(-L_1)/(L_1+L_3)}{L_1+L_2-(L_1^2/(L_1+L_3))} \\ \frac{L_1/(L_1+L_2)-1}{L_1+L_3-L_1^2/(L_1+L_3)} & \frac{(-L_1)/(L_1+L_2)}{L_1+L_3-L_1^2/(L_1+L_3)} & \frac{1}{L_1+L_3-L_1^2/(L_1+L_3)} \end{bmatrix}}^{B_c} \overbrace{\begin{bmatrix}P_1\\ P_2\\ P_3\end{bmatrix}}^{y_p}$$

$$\underbrace{\begin{bmatrix}x_3\\ x_2\\ x_1\end{bmatrix}}_{y} = \underbrace{\begin{bmatrix} 0 & 0 & 0 & -1 & -1 \\ 0 & 0 & 0 & 1 & 0 \\ 0 & 0 & 0 & 0 & 1 \end{bmatrix}}_{C_c} \underbrace{\begin{bmatrix}x_3\\ x_2\\ x_1\\ v_2\\ v_1\end{bmatrix}}_{\dot{x_c}} + \underbrace{\begin{bmatrix} 0 & 0 & 0 \\ 0 & 0 & 0 \\ 0 & 0 & 0 \end{bmatrix}}_{D_c} \underbrace{\begin{bmatrix}P_1\\ P_2\\ P_3\end{bmatrix}}_{y_p} \tag{16}$$

Deriving the state space model by hand is tedious, time consuming, and error prone (A_c for Figure 5 is a 13×13 matrix, see ESI). A MATLAB script was written to automate this process.

3.3 Combining Chip Model with Pump Model

The closed loop system also includes the pressure pump, which has its own dynamics as shown earlier. Typical volumetric flow rate through a microfluidic chip is in the order of μL per minute, and is well within the electro-pneumatic transducer flow capacity. Because of this, the pressure from each inlets are de-coupled (independent) from each other, and the pump state space model (A_p, B_p, C_p, D_p) can be obtained directly from its SISO transfer function (equation 3) using Canonical Realization.

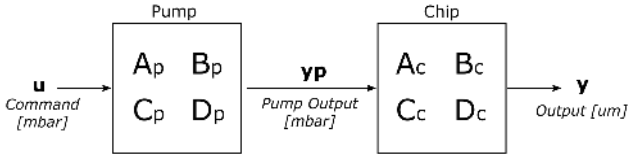

Fig. 6 Pump and Chip state space model connected in series.

The pressure pump model and chip model are then connected in series (figure 6), where the pump outputs act as chp inputs. Through block diagram manipulation, the combined plant state space model (A, B, C, D) is obtained through equation 17, where pump states x_p and chip states x_c combine to become x. For numerical values and the entire 25×25 matrices, please refer to ESI.

$$\overbrace{\begin{bmatrix} \dot{x_p} \\ \dot{x_c} \end{bmatrix}}^{\dot{x}} = \overbrace{\begin{bmatrix} A_p & \mathbf{0} \\ B_c C_p & A_c \end{bmatrix}}^{A} \overbrace{\begin{bmatrix} x_p \\ x_c \end{bmatrix}}^{x} + \overbrace{\begin{bmatrix} B_p \\ B_c D_p \end{bmatrix}}^{B} u$$

$$y = \underbrace{\begin{bmatrix} D_c C_p & C_c \end{bmatrix}}_{C} \underbrace{\begin{bmatrix} x_p \\ x_c \end{bmatrix}}_{x} + \underbrace{\begin{bmatrix} D_c D_p \end{bmatrix}}_{D} u \tag{17}$$

4 Controller Design

Without experimental data, it was unsure whether the state space model is valid, and designing a MIMO controller for an invalid plant model would have been a futile attempt. On the other hand, the plant model is marginally unstable, and a controller is necessary for stabilizing the system before any valuable data can be captured.

Faced with this dilemma, simple SISO controllers are designed instead, each treating the channel they control to be isolated from the rest of the channel network. Transient performance will obviously be compromised since coupling effects are not modelled, but with the advantage of feedback , these controllers should be able to stabilize the system at the very least.

4.1 Simplified Model

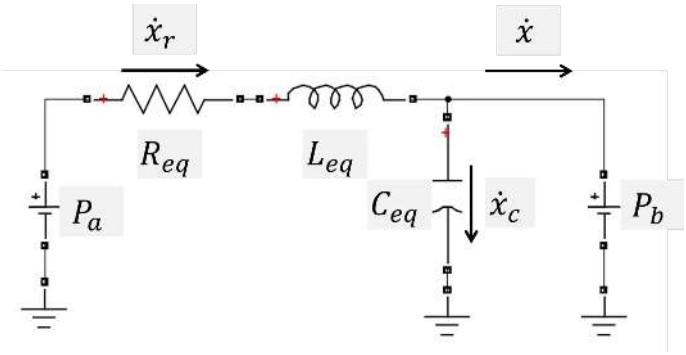

Fig. 7 Simplified circuit representation of an isolated channel

Figure 7 shows a circuit representing an isolated channel, where P_a, P_b are inlet pressures, and $\dot{x_r}, \dot{x_c}, \dot{x}$ are flow velocities of each circuit component. The governing equations are shown in equation 18, which is rearranged and Laplace transformed into equation 19. In the SISO case, downstream pressure P_b is treated as disturbance, allowing the $P_b(s)C_{eq}$ term to be removed. This results in the plant transfer function $P_{channel}$ which describe the dynamics of displacement $X(s)$ versus applied pressure $\triangle P(s)$. Table 3 contains a list of parameters for substituting into equation 20 to yield corresponding plant model for channel 1 and channel 2 in the T-junction.

$$\begin{aligned} P_a - P_b &= \dot{x_r} \cdot R_{eq} + \ddot{x_r} \cdot L_{eq} \\ P_b &= \frac{x_c}{C_{eq}} \\ \dot{x} &= \dot{x_r} + \dot{x_c} \end{aligned} \tag{18}$$

$$X(s) = \frac{1/L_{eq}}{s(s + R_{eq}/L_{eq})}(P_a(s) - P_b(s)) - P_b(s)C_{eq} \tag{19}$$

$$P_{channel} = \frac{X(s)}{\triangle P(s)} = \frac{1/L_{eq}}{s(s + R_{eq}/L_{eq})} \tag{20}$$

A closer look at $P_{channel}$ suggests that channel dynamics is marginally unstable. This matches the observation that given any constant inlet pressures, droplet and interface positions will likely drift away instead of hold still. In reality, capillary forces and non-uniform channel wall wetting create disturbance that either stabilize, or de-stabilize the system further. These effects, however, are treated as plant uncertainty, and counteracted once again by feedback.

The second order plant derived above is simple and convenient for controller design, but neglects capacitance effect entirely. A more complicated model is derived from figure 8. The governing equations and Laplace transforms are provided in equation 21 and 22. The result is a 4th order transfer function shown in equation 23. This 4th order plant is not used in designing controllers, but as an evaluation tool instead to analyse the closed-loop performance, and to test if the simpler model (equation 20) is trust worthy.

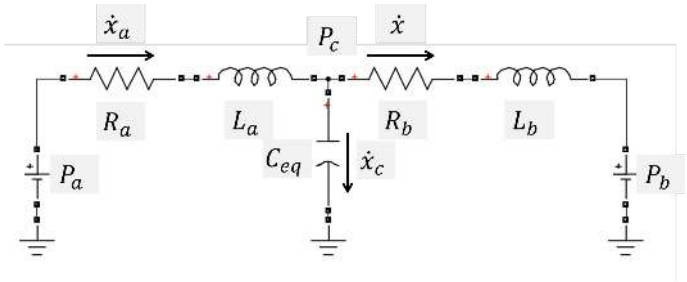

Fig. 8 A more accurate circuit representation of an isolated channel

$$\begin{aligned} P_a - P_c &= \ddot{x_a} \cdot L_a + \dot{x_a} \cdot R_a \\ P_c - P_b &= \ddot{x} \cdot L_b + \dot{x} \cdot R_b \\ P_c &= \frac{x_c}{C_{eq}} \\ \dot{x} &= \dot{x_a} - \dot{x_c} \end{aligned} \tag{21}$$

$$\begin{aligned} X(s) &= \frac{P_a(s) - P_b(s)}{\theta} - \frac{sC_{eq}L_a + C_{eq}R_a}{\theta} P_b(s) \\ \theta &= s^4(C_{eq}L_aL_b) + s^3(C_{eq}L_aR_a + C_{eq}L_bR_b) \\ &+ s^2(L_a + L_b + C_{eq}R_aR_b) + s(R_a + R_b) \end{aligned} \tag{22}$$

$$P_{channel} = \frac{X(s)}{\triangle P(s)} = \frac{1}{\theta} \tag{23}$$

In experiment, pressure pump and controller operate at $10Hz$. Between sampling, dyanmics that took place on chip will not be registered by the controller until the next sampling point. This discretization effect is approximated as a delay. In the laplace domain, a delayed function is $\mathscr{L}\{f(t-\tau)\} = e^{-s\tau}F(s)$. Using the Pade approximation, the exponent is approximated as a transfer function, and the delayed plant P_{delay} is acquired by setting $\tau = 0.5 \times SamplePeriod = 0.05$ (equation 24).

$$P_{delay} = e^{-s\tau} \approx \frac{1 - s\tau/2}{1 + s\tau/2} \tag{24}$$

4.2 Controller

Second order controllers are designed using pole placement technique to achieve closed-loop stability and disturbance rejection. A controller transfer function $C_{continuous}$is shown in equation 25, where T_i, T_d, T_a and K are controller parameters denoted in the Lead Lag compensator convention. The integrator (lack of constant term in the denominator polynomial) is critical for rejecting disturbance resulted from MIMO coupling effects. To describe dynamics of the overall feedback loop involving the plant, delay, and controller, equation 26 can be written. T_{ry} is the closed loop transfer function representing reference r to output y response.

$$C_{continuous} = K\frac{T_is + 1}{s}\frac{T_ds + 1}{T_as + 1} \tag{25}$$

$$T_{ry} = \frac{y(s)}{r(s)} = \frac{P_{channel}P_{delay}C_{continuous}}{1 + P_{channel}P_{delay}C_{continuous}} \tag{26}$$

The closed-loop dynamics is highly dependent on the roots of the denominator polynomial of T_{ry}. By re-arranging plant transfer functions and controller transfer functions into equation 27 and equation 28, the closed-loop denominator polynomial can be written as equation 29, where $\triangle_5, \triangle_4, etc$ are coefficients obtained by forming a polynomial with the desired roots.

$$P_{channel}P_{delay} = \frac{a_3s^3 + a_2s^2 + a_1s + a_0}{s^3 + b_2s^2 + b_1s + b_0} \tag{27}$$

$$C_{continuous} = \frac{c_2s^2 + c_1s + c_0}{d_2s^2 + d_1s} \tag{28}$$

$$\overbrace{\begin{bmatrix} 1 & 0 & a_3 & 0 & 0 \\ b_2 & 1 & a_2 & a_3 & 0 \\ b_1 & b_2 & a_1 & a_2 & a_3 \\ b_0 & b_1 & a_0 & a_1 & a_2 \\ 0 & b_0 & 0 & a_0 & a_1 \end{bmatrix}}^{Sylvester} \begin{bmatrix} d_2 \\ d_1 \\ c_2 \\ c_1 \\ c_0 \end{bmatrix} = \begin{bmatrix} \triangle_5 \\ \triangle_4 \\ \triangle_3 \\ \triangle_2 \\ \triangle_1 \end{bmatrix}$$

$$desiredpolynomial = \triangle_5s^5 + \triangle_4s^4 + \triangle_3s^3 + \triangle_2s^2 + \triangle_5s \tag{29}$$

Controller parameters c_2, d_2, etc is obtained by inverting the Sylvester matrix. The controllers $C_{continuous}$ are then discretized by substituting $s = \frac{2}{SamplePeriod}\frac{z-1}{z+1}$. The general form of this discretized controller is shown in equation 30, and the discrete parameters for channel 1 and channel 2 controllers are listed in table 3. Finally, difference equation (equation 31) is obtained from $C_{discrete}$, and used to calcualte appropriate command u based on previous errors e. In the experiment set up, a script was written to translate equation 31 into PID form, so small intuitive tuning could be performed during testing.

$$\begin{aligned} C_{discrete} &= \frac{u(z)}{e(z)} = \frac{f_2z^2 + f_1z + f_0}{g_2z^2 + g_1z + g_0} \\ SamplePeriod &= 0.1 \end{aligned} \tag{30}$$

$$u_{[t]} = \frac{f_2}{g_2}e_{[t]} + \frac{f_1}{g_2}e_{[t-0.1]} + \frac{f_0}{g_2}e_{[t-0.2]} - \frac{g_1}{g_2}u_{[t-0.1]} - \frac{g_0}{g_2}u_{[t-0.2]} \tag{31}$$

To investigate noise and disturbance rejectioni ability of the closed-loop system, the sensitivity function T_{ny} and disturbance transfer function T_{dy} is derived in equation 32 and 33.

$$T_{ny} = \frac{y(s)}{n(s)} = -\frac{1}{1 + P_{channel}P_{delay}C_{continuous}} \tag{32}$$

$$T_{dy} = \frac{y(s)}{d(s)} = -\frac{P_{channel}P_{delay}}{1 + P_{channel}P_{delay}C_{continuous}} \tag{33}$$

The MIMO nature of droplet dynamics dictates that output(displacement) in one channel will cause noise in other channels. It is therefore important for T_{ny} of channel 1 to operate at different frequency from T_{ry} of channel 2, such that two closed-loop systems do not resonate. Figure 9A) and B) confirms that frequency response of T_{ny} and T_{ry} do not overlap until their magnitude is less than 0 dB. In addition, figure 9D shows that T_{dy} approach 0 magnitude at low frequency, attenuating any steady-state disturbance.

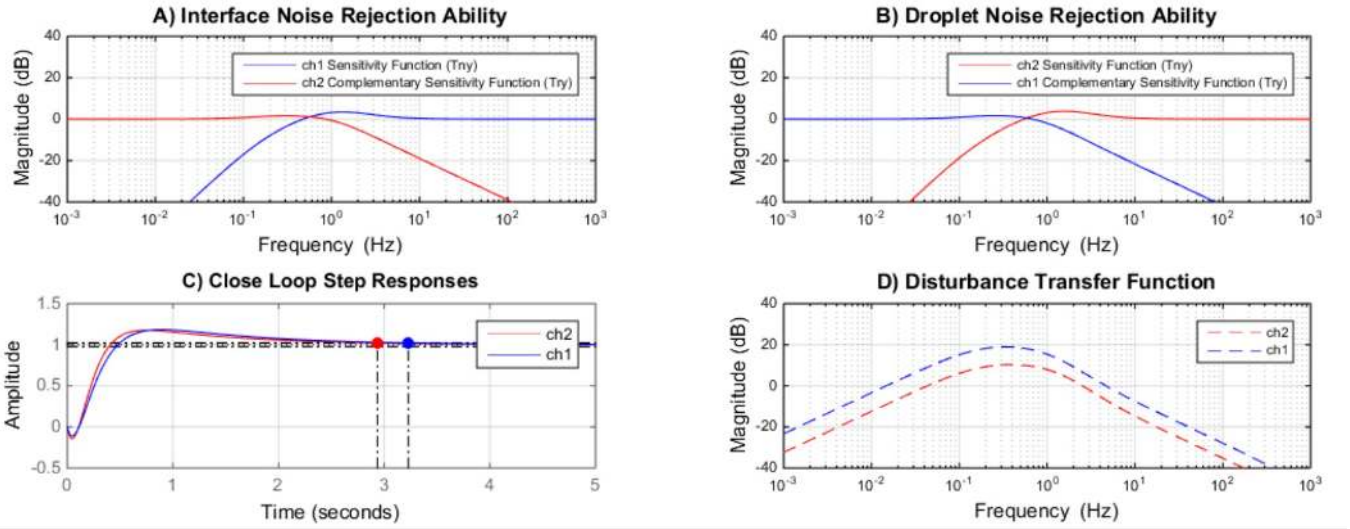

Fig. 9 Predicted closed-loop behaviour. A,B) Controllers are designed to respond to reference and noise at different frequency range, in order to prevent resonance due to coupling effects. C) Droplet and interface are designed to reach their desired position within 3 seconds and over-shoot less than 20%. D) Disturbance transfer function for both channel 1 and channel 2 approach zero at low frequency (i.e.steady state), demonstrating the controller's ability to reject static bias and disturbance.

Table 3 Controller Design Parameters

Parameters	Channel 1 (slow)	Channel 1	Channel 2
R_{eq}	$R_1+(R_2R_3)/(R_2+R_3)$	$<-$	$R_2+(R_3R_1)/(R_3+R_1)$
L_{eq}	$L_1+(L_2L_3)/(L_2+L_3)$	$<-$	$L_2+(L_3L_1)/(L_3+L_1)$
C_{eq}	$C_1+C_2+C_3$	$<-$	$C_1+C_2+C_3$
R_a	R_1	$<-$	R_2
L_a	L_1	$<-$	L_2
R_b	$(R_2R_3)/(R_2+R_3)$	$<-$	$(R_3R_1)/(R_3+R_1)$
L_b	$(L_2L_3)/(L_2+L_3)$	$<-$	$(L_3L_1)/(L_3+L_1)$
f_2	0.1693	0.4191	0.4975
f_1	−0.1912	−0.4352	−0.5603
f_0	0.03142	0.7018	0.09201
g_2	1	1	1
g_1	−0.9707	−0.5727	−0.8865
g_0	−0.02932	−0.4273	−0.1135

5 Experiment

The experiment procedures are as follow. First, the $500\mu m$ cross-hair (part of the chip) was used to calibrate pixel-to-micron scaling. Image processing and pressure pump were then switched on. Droplets were generated manually by changing the inlet pressures according to a specific time-series. Once the droplet fell within image processing regions, the controllers were enabled. From there on, droplet position and interface position was held automatically stationary, until further user request.

To prevent sudden changes in applied pressures during transition from open-loop to closed-loop, the controller command u are implemented as in equation 34. For inlet 1, command signal u_1 is aggregated into the open-loop pressure as . Also, since there are three input pressures but only two degrees of freedom in the system, the second command signal u_2 is shared between inlet 2 and inlet 3.

$$P_{1,closed-loop} = P^{Initial}_{1,open-loop} + u_1$$

$$P_{2,closed-loop} = P^{Initial}_{2,open-loop} + 0.5 \times u_2$$

$$P_{3,closed-loop} = P^{Initial}_{3,open-loop} - 0.5 \times u_2 \quad (34)$$

5.1 Droplet Position Control (Trapping)

Figure 10 shows user requesting independent changes in droplet position and interface position. In the experiment, a $500\mu m$ step change in droplet position was demanded by the user, the controller in channel 2 proceeded to move the droplet to the right. At that moment, since controllers were SISO in nature, channel 1 controller could not anticipate actions of channel 2 controller, hence the interface was disturbed. In less than 3 seconds, the droplet settled to its new position, while channel 1 controller reacted to the error induced by disturbance, and returned the interface to its initial position. Next, a $500\mu m$ interface step down is demanded. This time, channel 1 controller proceeded to lower the interface, while channel 2 controller reacted to compensate for the disturbed droplet. In less than 3 seconds, both interface and droplet were at their new positions. Please refer to ESI for the full video of this experiment.

The authors are aware of the high overshoot in both droplet and interface displacement. While MIMO controllers will help with suppression, it should be noted that applying big step request is not common in practice, except for during system testing. Rather, smooth trajectories or a series of small steps would be used (demonstrated below), in which case overshoot will be much less pronounced.

5.2 Merging and Splitting

The same controllers can be used to merge and split droplets. In figure 11A the experiment started with two droplets situated in channel 2. Average of the two droplet centroids was used for controller feedback. First, one droplet was moved across the T-junction (not shown), then the interface was requested to move

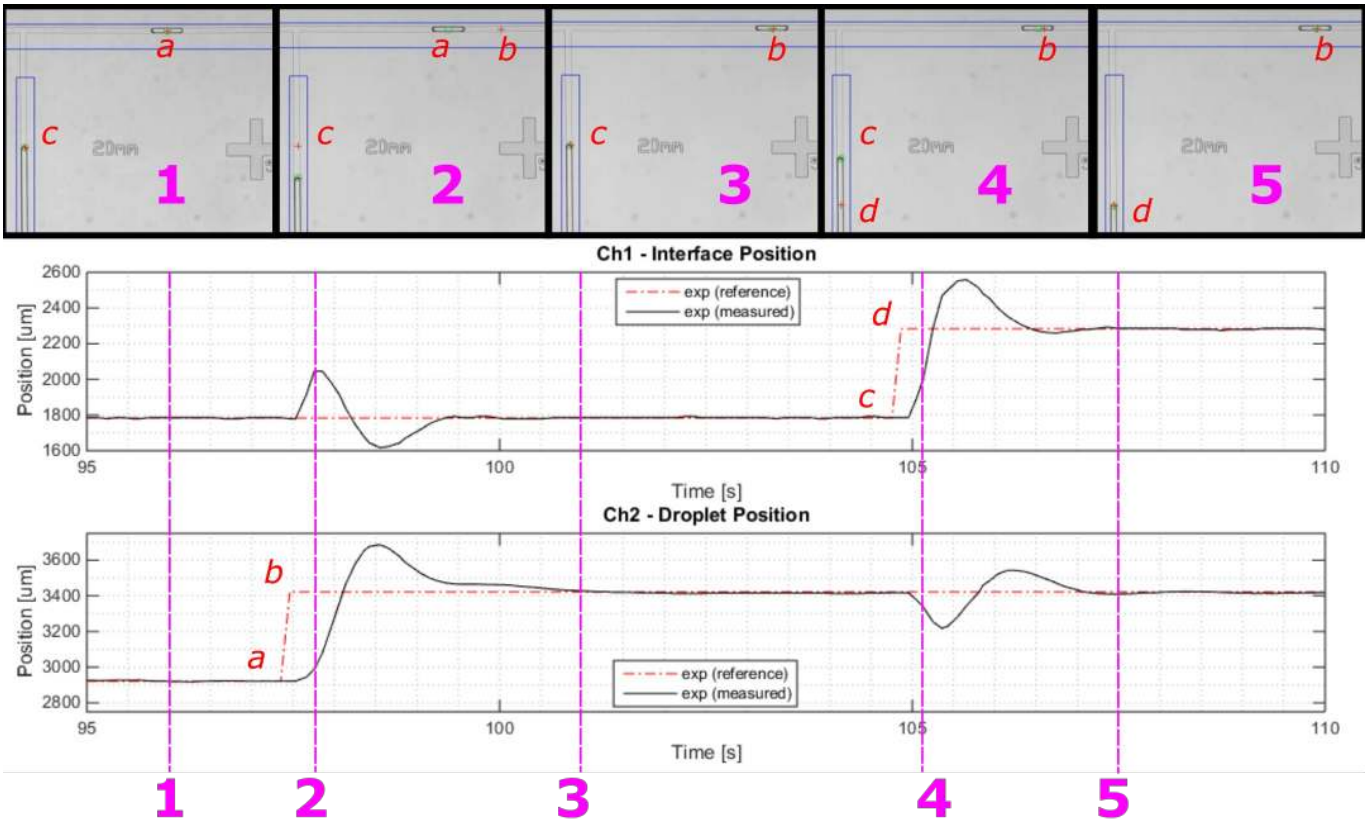

Fig. 10 Controlled step change of droplet and interface position with SISO controllers. 1) Interface and droplet are at their initial positions. 2) User request droplet to move to *b*, coupling effects results in interface being disturbed. 3) Droplet moved to *b*, interface recovered initial position. 4) User request interface to move to *d*, droplet is slightly disturbed. 5) Interface and droplet both at their new positions.

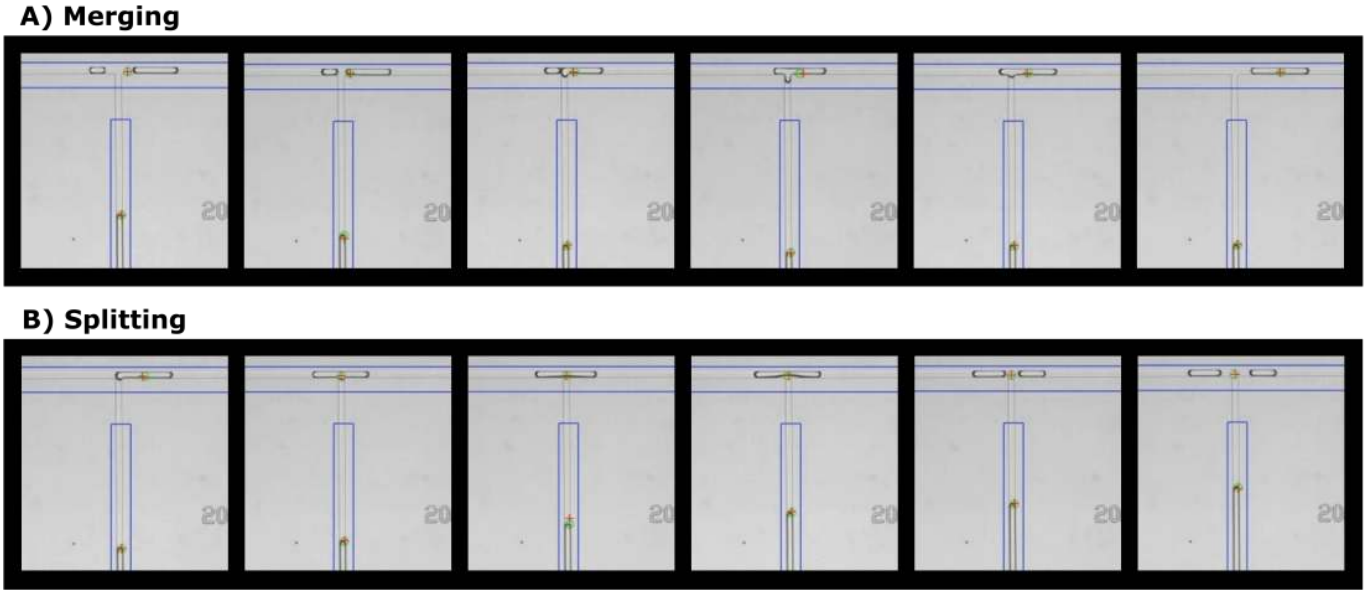

Fig. 11 Montage showing the merging and splitting operations

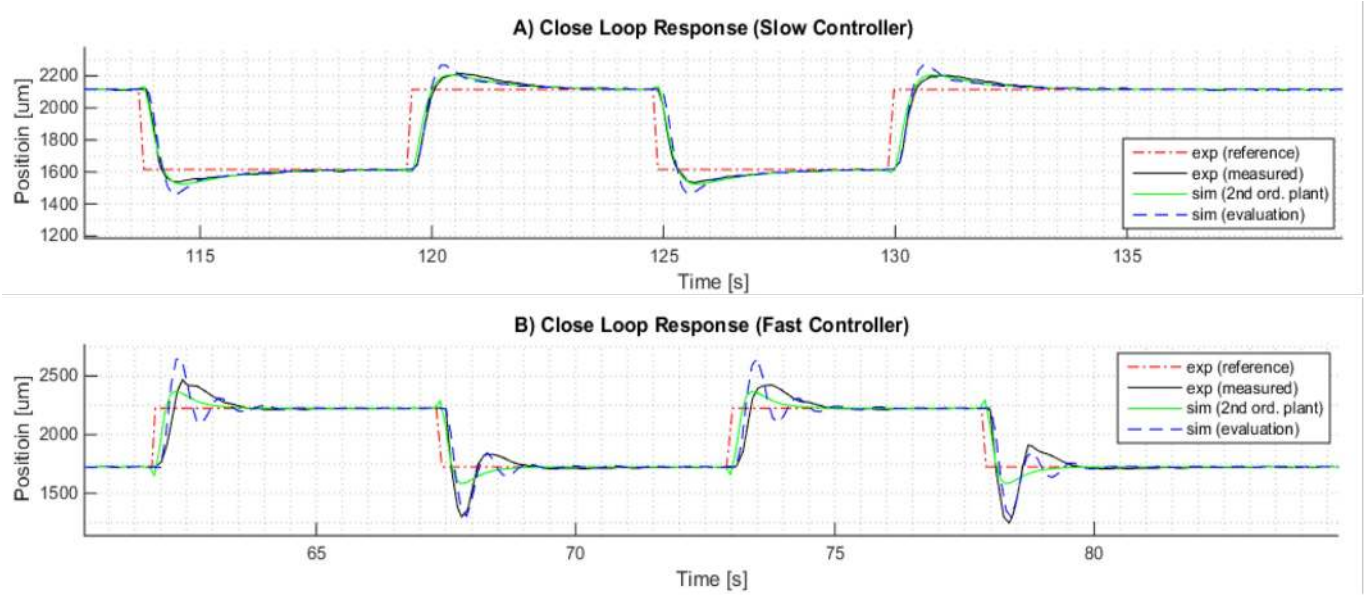

Fig. 12 Closed-loop model prediction vs. experiment data. A) With a slow responding controller, the simplified 2nd order plant does a good job of simulating interface behaviour. B) With a fast responding controller, 2nd order plant under-predicts the over-shoot and settling-time, while the evaluation model (4th order plant)better matches experiment. Notice that system response is different between step-up and step-down, suggesting that non-linear dynamics exist, but is never-the-less stabilized by the controllers.

down, removing oil that separated the two droplets. The two droplets merged after touching, and was moved away from the T-junction afterwards. In figure 11B the experiment started with a single droplet in channel 2. The droplet was requested to move to the middle of the T-junction, interface was then requested to move up. While being T-boned, the droplet would try to escape by either slipping to the right or left, but channel 2 controller compensated through-out to keep the droplet in place. Please refer to ESI for full video of this experiment.

Using this procedure, droplets can be split and merged repeatedly. And the splitting accuracy is roughly estimated to be 10%. The daughter droplets volume is a result of the mother droplet position as it is slitted, so improving controller performance should lead to higher splitting accuracy. Splitting can also be performed in $100\mu m$ channels as oppose to the $50\mu m$ shown, please refer to ESI for video clip.

6 Analysis

6.1 SISO Model Validation

In order to validate the SISO models (equation 20 and 23), it is necessary to obtain coupling-free data. In these experiments, only channel 1 controller was active, and the interface position was recorded and compared to model predictions. Data obtained from experiment with the slow controller and fast controller (listed in table 3) are shown in figure 12. Please refer to ESI for videos of these single channel experiments.

Experimental data are compared to two sets of simulation predictions. The first simulation uses the 2nd order plant (equation 20) and a continuous controller (equation 25), while the second simulation uses the 4th order plant (equation 23) and a discrete controller (equation 30). Referring to figure 12A) when the slow controller is used, both simulations capture the response and settling time well, with the 4th order plant system slightly over-predicting overshoots. In figure 12B) with the fast controller in place, only the system with the 4th order plant matches the experiment result. This suggests that our design approach is suitable for designing controllers with moderate performance, but would fail to predict system dynamics when sped up. Note that at high speeds, discrepancy results from the pressure pump behaving asymmetrically, where response to a downward step is different from response to an upward step (more overshoot and oscillations).

6.2 MIMO Model Validation

Although SISO closed-loop system has been constructed, MIMO closed-loop system has yet to be derived. Therefore, the dilemma stated in section 4 remains. In order to prevent the MIMO plant model (equation 17) from diverging during simulation, a Kalman filter (figure 14) is added. Base on experiment command $u_1, u_2, ..., u_m$ and measured output $y_1, y_2, ..., y_p$, the Kalman filter estimate system states $x_1, x_2, ..., x_n$ which are often impractical to measure. By including disturbance $d_1, d_2, ..., d_m$ as states, the Kalman filter computes the amount of disturbance that is needed to "nudge" the plant model into matching experiment data. Note that in previous sections, disturbance represents coupling effects unaccounted for in a SISO system. Here, coupling effects are modelled, and disturbance represents differences between model and reality, and is therefore a main indication of model validity. The discrete augmented state space model (A_z, B_z, C_z, D_z) including disturbance as states are shown in equation 35, where w_{k-1} and v_k represent modelling noise and sensor noise (a uniform distribution based on image resolution).

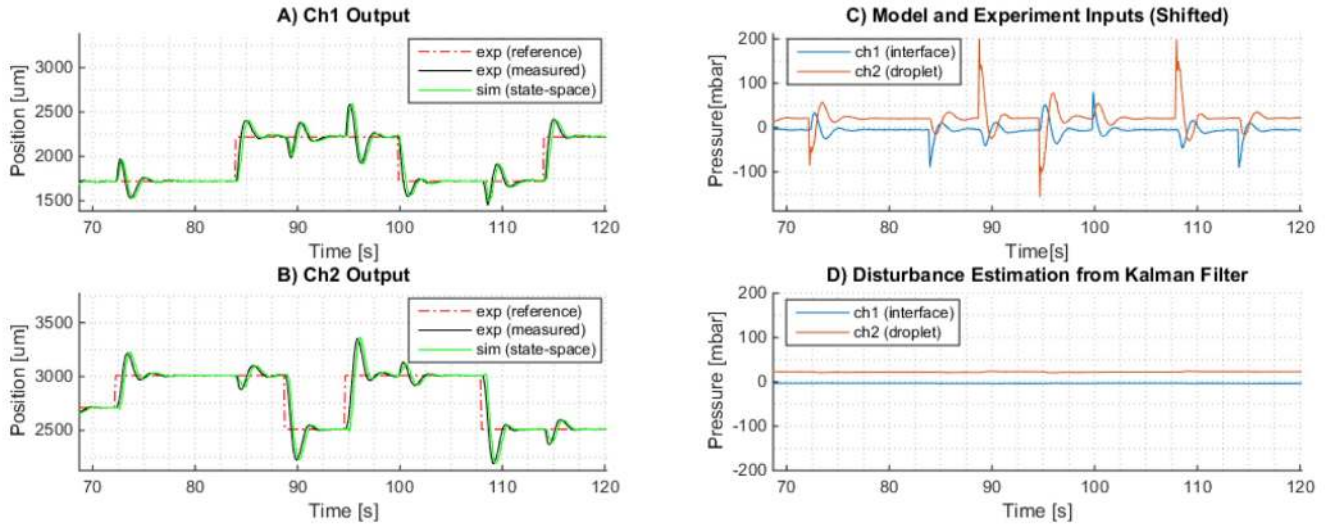

Fig. 13 State space plant model prediction vs experiment data. A,B) Droplet and interface position predicted by model closely matches experiment data, coupling effect is successfully captured. C) Controller command recorded during experiment is fed into plant model as inputs. D) Disturbance estimations from Kalman filter (representing unmodelled dynamics).

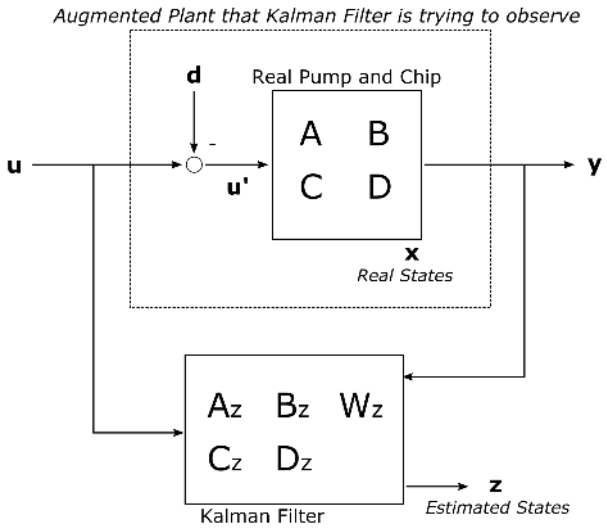

Fig. 14 Estimate Disturbance using Kalman Filter

$$\overbrace{\begin{bmatrix} x_k \\ d_k \end{bmatrix}}^{z_k} = \overbrace{\begin{bmatrix} A & -B \\ \mathbf{0} & \mathbf{1} \end{bmatrix}}^{A_z} \overbrace{\begin{bmatrix} x_{k-1} \\ d_{k-1} \end{bmatrix}}^{z_{k-1}} + \overbrace{\begin{bmatrix} B \\ \mathbf{0} \end{bmatrix}}^{B_z} u_{k-1} + \overbrace{\begin{bmatrix} \mathbf{0} \\ \mathbf{1} \end{bmatrix}}^{W_z} w_{k-1}$$

$$\hat{y_k} = \underbrace{\begin{bmatrix} C & \mathbf{0} \end{bmatrix}}_{C_z} \underbrace{\begin{bmatrix} x_k \\ d_k \end{bmatrix}}_{z_k} + \underbrace{\begin{bmatrix} D \end{bmatrix}}_{D_z} u_k + v_k$$

$$SamplePeriod = 0.1 \tag{35}$$

Figures 13A) and B) show the simulation output vs. experiment data. As expected, the coupling effects are well captured. More importantly, in figure 13D, the Kalman disturbance estimates are essentially constant. Since disturbance has the same unit as command ($u' = u - d$) as seen in figure 14, comparison between figure 13C and figure 13D implies that the MIMO plant model captures droplet dynamics rather well, and only needs some static bias corrections.

Possible causes of the static bias include surface tension across water-oil interfaces, capillary forces between air-water interfaces in the pump reservoir, as well as gravitational forces. In practice, MIMO controller with state feedback and integral action will compensate for such bias.

6.3 Performance Limitations

In this last section, we briefly comment on the performance limitations of the microfluidic channel network system. Pump dynamics will be ignored from here on.

Poles of a system s_p can be found by solving the determinant in equation 36. They are special values of s at which the system produce outputs even when inputs are absent. Zeros of a system s_z can be found by solving the determinant of the Rosenbrock's system matrix as shown in equation 37, and corresponds to values of s when outputs are absent but inputs are not.

$$\left| Is_p - A_c \right| = 0 \tag{36}$$

$$\begin{vmatrix} Is_z - A_c & B_c \\ -C_c & D_c \end{vmatrix} = 0 \tag{37}$$

Rule-of-thumb in controller design (equation 38) suggests that, in the absence of Open Right Hand Plane (ORHP) poles and zeros cancellation, the plant can be stabilized, which is true in our case. Further more, to achieve "strong stability" and good performance, controllers must be designed such that closed-loop bandwidth BW_{cl} is larger than any ORHP poles and smaller than any ORHP zeros.

$$2 \times max(s_p^{ORHP}) < BW_{cl} < 0.5 \times min(s_z^{ORHP}) \tag{38}$$

For the chip model derived in section 3.2, the poles and zeros are calculated and listed in equation 39. While the first three poles are in ORHP (which contributes to the marginal instability), all the ORHP zeros are at infinity. Hence, there are essentially no limitation on closed-loop performance. A more rudimentary investigation of performance limitation can be found in chapter 6 of Skogestad[23].

$$s_p = \begin{bmatrix} 0 \\ 0 \\ 0 \\ -6.25e05 \\ -6.40e05 \\ -1.33e04 + 4.71e04i \\ -1.33e04 - 4.71e04i \\ -8.52e02 + 2.60e03i \\ -8.52e02 - 2.60e03i \\ -1.56e03 + 1.42e03i \\ -1.56e03 - 1.42e03i \\ -1.49e03 + 1.31e03i \\ -1.49e03 - 1.31e03i \end{bmatrix} \quad s_z = \begin{bmatrix} \infty \\ \infty \\ \infty \\ -9.38e18 \\ -2.28e-10 \\ \infty \\ \infty \\ \infty \\ \infty \\ \infty \\ \infty \\ \infty \\ \infty \\ \infty \\ \infty \\ \infty \end{bmatrix} \tag{39}$$

Practically, very fast closed-loop response is infeasible. Figure 15 shows the frequency response of a symmetric T-junction (equal channel dimensions and fluid properties). For an oil filled junction, droplets displacements are attenuated above 3 Hz. To achieve accurate droplets motions at higher frequencies will require very high inlet pressures actuation, which might led to pump saturation or chip failure. This low-pass filter behaviour changes with fluid properties and channel dimensions, and could be investigated in the future.

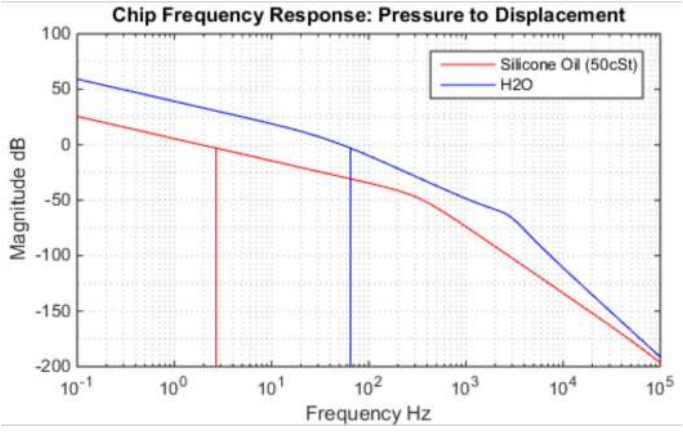

Fig. 15 Inlet 1(pressure) to Channel 1(displacement) Frequency Response, extracted from MIMO chip model of a symmetric T-junction.

7 Conclusions

In conclusion, we have demonstrated the benefits of applying controls theory to droplet microfluidics. Droplets and interface positions can be held steady or moved independently, regardless of channel dimensions. Splitting and merging can be performed at T-junctions, and the procedure is effortless and repeatable. We provided a state space model that successfully captures droplet dynamics in a T-junction, and can be scaled up to describe more complicated microfluidic channel networks. We also demonstrated the procedures for designing controllers to achieve closed-loop stability and moderate performance.

In the future, MIMO controllers should be designed and implemented, which would drastically improve performance by anticipating coupling effects. Performance will also improve by eliminating the bottle neck $10Hz$ sampling period. In addition, new droplet generation models would need to be created, since existing models seldom describe droplet formation in a relatively static fluid field.

8 Acknowledgement

The authors would like to thank Natural Science and Engineering Research Counsil Canada, and Canada Foundation for Innovation for the grants awarded to Dr. Ren, as well as Professor Kaan Erkorkmaz at the University of Waterloo for providing many insights in controls theory.

References

1 L. Mazutis, A. F. Araghi, O. J. Miller, J.-C. Baret, L. Frenz, A. Janoshazi, V. Taly, B. J. Miller, J. B. Hutchison, D. Link *et al.*, *Analytical chemistry*, 2009, **81**, 4813–4821.

2 A. M. Klein, L. Mazutis, I. Akartuna, N. Tallapragada, A. Veres, V. Li, L. Peshkin, D. A. Weitz and M. W. Kirschner, *Cell*, 2015, **161**, 1187–1201.

3 I. Shestopalov, J. D. Tice and R. F. Ismagilov, *Lab on a Chip*, 2004, **4**, 316–321.

4 T. Rossow, J. A. Heyman, A. J. Ehrlicher, A. Langhoff, D. A. Weitz, R. Haag and S. Seiffert, *Journal of the American Chemical Society*, 2012, **134**, 4983–4989.

5 S. K. Cho, H. Moon and C.-J. Kim, *Microelectromechanical Systems, Journal of*, 2003, **12**, 70–80.

6 A. M. Pit, M. H. Duits and F. Mugele, *Micromachines*, 2015, **6**, 1768–1793.

7 Y.-C. Tan, J. S. Fisher, A. I. Lee, V. Cristini and A. P. Lee, *Lab on a Chip*, 2004, **4**, 292–298.

8 G. Christopher, J. Bergstein, N. End, M. Poon, C. Nguyen and S. L. Anna, *Lab on a Chip*, 2009, **9**, 1102–1109.

9 K. Churski, P. Korczyk and P. Garstecki, *Lab Chip*, 2010, **10**, 816–818.

10 K. Churski, T. S. Kaminski, S. Jakiela, W. Kamysz, W. Baranska-Rybak, D. B. Weibel and P. Garstecki, *Lab on a Chip*, 2012, **12**, 1629–1637.

11 T. S. Kaminski, S. Jakiela, M. A. Czekalska, W. Postek and P. Garstecki, *Lab on a Chip*, 2012, **12**, 3995–4002.

12 S. Jakiela, T. S. Kaminski, O. Cybulski, D. B. Weibel and P. Garstecki, *Angewandte Chemie*, 2013, **125**, 9076–9079.

13 E. Miller, M. Rotea and J. P. Rothstein, *Lab on a Chip*, 2010, **10**, 1293–1301.

14 W. Zeng, S. Li and Z. Wang, *Sensors and Actuators A: Physical*, 2015, **233**, 542–547.

15 B. Kuczenski, P. R. LeDuc and W. C. Messner, *Lab on a Chip*, 2007, **7**, 647–649.
16 Y. Kim, P. LeDuc and W. Messner, *Control Systems Technology, IEEE Transactions on*, 2013, **21**, 203–211.
17 X. Niu, M. Zhang, S. Peng, W. Wen and P. Sheng, *Biomicrofluidics*, 2007, **1**, 044101.
18 M. D. Armani, S. V. Chaudhary, R. Probst and B. Shapiro, *Microelectromechanical Systems, Journal of*, 2006, **15**, 945–956.
19 A. Shenoy, M. Tanyeri and C. M. Schroeder, *Microfluidics and Nanofluidics*, 2015, **18**, 1055–1066.
20 R. L. Woods and K. L. Lawrence, *Modeling and simulation of dynamic systems*, Prentice-Hall, 1997.
21 G. F. Franklin, J. D. Powell and A. Emami-Naeini, *Feedback control of dynamics systems*, Prentice-Hall, 1994.
22 D. Qin, Y. Xia and G. M. Whitesides, *Nature protocols*, 2010, **5**, 491–502.
23 S. Skogestad and I. Postlethwaite, *Multivariable feedback control: analysis and design*, Wiley New York, 2007, vol. 2.